Article

Critical Quantum Metrology in the Non-Linear Quantum Rabi Model

Zu-Jian Ying [1,*] , Simone Felicetti [2,*] , Gang Liu [1] and Daniel Braak [3,*]

1   School of Physical Science and Technology, Lanzhou University, Lanzhou 730000, China
2   Institute for Complex Systems, National Research Council (ISC-CNR), 00185 Rome, Italy
3   EP VI and Center for Electronic Correlations and Magnetism, University of Augsburg,
    86135 Augsburg, Germany
*   Correspondence: yingzj@lzu.edu.cn (Z.-J.Y.); felicetti.simone@gmail.com (S.F.);
    daniel.braak@physik.uni-augsburg.de (D.B.)

Abstract: The quantum Rabi model (QRM) with linear coupling between light mode and qubit exhibits the analog of a second-order phase transition for vanishing mode frequency which allows for criticality-enhanced quantum metrology in a few-body system. We show that the QRM including a nonlinear coupling term exhibits much higher measurement precisions due to its first-order-like phase transition at *finite* frequency, avoiding the detrimental slowing-down effect close to the critical point of the linear QRM. When a bias term is added to the Hamiltonian, the system can be used as a fluxmeter or magnetometer if implemented in circuit QED platforms.

1. Introduction

The high susceptibility developed by critical systems [1,2] in proximity of phase transitions is a compelling resource for metrology and sensing. For example, relevant scientific and technological applications of critical systems are bubble chambers [3] and transition-edge sensors [4]. However, even when these devices have a quantum working principle, they follow a classical sensing strategy. However, it is well known that quantum properties such as squeezing and entanglement can be used to outperform any classical sensing protocol [5]. As systems in proximity of quantum phase transitions [6] are expected to have a highly nonclassical behavior, it is natural to analyze the critical systems with a quantum-metrology perspective. In the last decade, various theoretical works have introduced different protocols able to leverage quantum critical phase transitions to achieve a fundamental advantage over classical sensing strategies [7–13]. However, an often-neglected fundamental hindrance limits the performances of critical quantum sensors: The diverging susceptibility is counterbalanced by the critical slowing down, which implies an extremely long protocol duration time. Only very recently it has been shown that, counterintuitively, even in the presence of the critical slowing down, the optimal limit of precision can be achieved [14]. Indeed, under standard assumptions, critical protocols can achieve the Heisenberg scaling—a quadratic growth of parameter-estimation precision—both with respect to the number of probes and with respect to the measurement time. Furthermore, a recent theoretical work [15] demonstrated that the optimal limits of precision can be achieved using finite-component phase transitions [16–28], which are criticalities that take place in quantum optical systems where the thermodynamic limit is replaced by a scaling of the system parameters [20,29–34]. Critical quantum sensors can then also be implemented with controllable small-scale quantum devices, without requiring the control of complex many-body systems. These results have prompted an intense research effort dedicated to designing efficient protocols [35–51] in terms of high estimation precision and

limited measurement time, and which can be implemented with experimentally feasible operations. Practical applications in quantum magnetometry and superconducting-qubit readout were also been proposed [52].

Critical quantum metrology protocols can be divided into two main approaches. The *static* approach [7–11,14,15,42–48,53] consists of bringing the system in an equilibrium state that depends on an external perturbation (such as a magnetic field). Such equilibrium states can be represented by the ground state reached during an adiabatic sweep, or by the steady-state achieved after a long-time evolution in a driven-dissipative setting. When the system is brought in proximity of the phase transition, one can obtain a very precise estimate of the parameter by measuring an observable on the equilibrium state. In contrast, the *dynamical* approach [12,13,36] consists of preparing the probe in a known state to then apply the perturbation and monitor the system time evolution, which can also have a critical dependence on the system parameters. Recent results obtained with spin systems and finite-component transitions suggest [14] that the dynamical and equilibrium approaches have a similar scaling of the estimation precision in the thermodynamic (or parameter-scaling) limit. However, the dynamical approach can achieve a constant factor advantage over static protocols [36], and it can allow super-Heisenberg scaling in collective light–matter interaction models [51]. For fully connected models, it has recently been shown that a continuous connection [54] can be drawn between the static and dynamical approaches, identifying universal time-scaling regimes.

In the design of critical quantum sensing protocols, a variety of physical models were considered, such as many-body spin systems [14], the ensemble of emitters coupled to cavity modes [10], single atom-cavity models [15,36], and nonlinear quantum resonators [52]. To date, except for a few exceptions, most studies have focused on the parameter regime defined by thermodynamic or parameter-scaling limits, where an effective analytical description can be derived. When considering finite-component phase transition, the most widely studied case is the quantum Rabi model (QRM) [55–57], composed of a two-level atom coupled to a single quantum harmonic mode. This model undergoes a second-order critical phase transition in the slow-resonator limit [16–20,26–28], where the frequency of the mode and the coupling strength are sent to zero with a given scaling law. Focusing on the scaling limit, one can obtain interesting results on the growth of the estimation precision in terms of fundamental resources such as the size of probe systems or photon number, however, to assess the actual precision of practical protocols, finite values of the parameters must be considered.

In this work, we propose quantum critical sensing protocols based on a generalization of the quantum Rabi model which includes a nonlinear (two-photon) coupling term and a transversal spin bias. The linear and nonlinear interactions lead to a ground state whose dependence on the linear coupling is much stronger at the critical value, entailing the equivalent of a first-order quantum phase transition. We consider the static approach where an adiabatic sweep is used to bring the system in proximity of criticality and we perform a numerical analysis which is not limited to the scaling regime. We show that adding the nonlinear coupling and the bias improves the protocol efficiency in different ways: (1) higher estimation precision, as measured by an increase in the quantum Fisher information; (2) faster adiabatic sweep and so shorter protocol duration time, due to the larger energy gap for finite values of physical parameters; (3) an extended range of the efficient sensing region, as the position of the critical point can be tuned in the space of parameters; (4) a less challenging requirement on the implementation of the slow-resonator limit. The considered model can be feasibly implemented with atomic [58–61] and solid-state [62–64] quantum devices with currently available technology.

2. Model

The nonlinear QRM with bias is described by the Hamiltonian [58,65]

$$
\begin{aligned}
H &= H_0 + H_t + H_\epsilon, \\
H_0 &= \omega a^\dagger a + \frac{\Omega}{2}\sigma_x + g_1\sigma_z(a^\dagger + a), \\
H_t &= g_2\sigma_z\big[(a^\dagger)^2 + a^2\big], \quad H_\epsilon = -\epsilon\sigma_z,
\end{aligned}
\tag{1}
$$

where $\sigma_{x,y,z}$ are Pauli matrices and $a^\dagger$ (a) creates (annihilates) a bosonic mode with frequency ω. The term proportional to Ω corresponds to tunneling between two states of the flux qubit in circuit QED implementations [62,66], or to the electronic-level splitting in trapped-ion implementations [59]. The strengths of linear and nonlinear couplings are denoted by g_1 and g_2 respectively. The bias term H_ϵ can be easily tuned by a bias current or by a static magnetic or electric field, depending on the implementation. In the slow-resonator limit $\omega \to 0$, the model exhibits the analogue of both second-order and first-order phase transitions as the thermodynamic limit in a many-body system is simulated here through the infinitesimal level spacing [65]. At finite frequencies, the discontinuities in the parameter dependence of expectation values are rounded off but show remnants of criticality. It should be noted that the parity symmetry of the linear QRM (H_0) is broken by H_t and H_ϵ. Notice that we are considering a Hamiltonian model, neglecting the effects of decoherence and dissipation. This allows us to focus on the role played by the two-photon coupling and bias terms, with respect to the standard quantum Rabi model. In practice, this implies that the metrological performance analyzed here is strictly valid within the coherence time of potential experimental implementations. In a recent experiment [67] with circuit-QED devices, it was shown that Schrödinger cat states can be generated using an implementation of the quantum Rabi model operated at criticality. The generation of these highly nonclassical states shows that the purely quantum dynamics generated by critical systems can indeed be applied in quantum-information tasks.

3. Relation between Transition Order and Accuracy

To discuss the difference between the linear ($g_2 = 0$) and nonlinear ($g_2 \neq 0$) cases for quantum metrology, let us start with zero bias $\epsilon = 0$. The model has a phase transition in the low-frequency limit $\omega \to 0$ at the critical point $g_1 = |g_{1c}| = |g_s|\sqrt{1 - g_2^2/g_t^2}$ [65,68] with $g_s = \sqrt{\omega\Omega}/2$ [17,19], and $g_t = \omega/2$ is the critical value of g_2 beyond which the Hamiltonian (1) is no longer self-adjoined and becomes unphysical [59,69–73]. The transition in this limit is second-order-like at $g_2 = 0$ [17–20,26–28] and first-order-like at finite g_2 [65,68]. The precision (signal-to-noise ratio) of any experimental estimation of one of the parameters λ in (1) is bound by $\mathcal{I}_\lambda^{1/2}$ [74], where $\mathcal{I}_\lambda$ is the quantum Fisher information [14,74,75], which takes the following form for pure states

$$
\mathcal{I}_\lambda(|\psi\rangle) = 4\Big(\langle\psi'(\lambda)|\psi'(\lambda)\rangle - |\langle\psi'(\lambda)|\psi(\lambda)\rangle|^2\Big),
\tag{2}
$$

where $'$ denotes the derivative of the ground state (GS) $|\psi(\lambda)\rangle$ of H in (1) with respect to λ. Obviously, a higher QFI means a higher measurement precision.

The Hamiltonian H has several parameters that can drive a phase transition. Let us begin with the linear coupling g_1 and set $\lambda = g_1/\Omega$ with Ω fixed. λ and $\mathcal{I}_\lambda$ are thus dimensionless. In Figure 1a, we compare the QFI for first- and second-order scenarios, as calculated with exact diagonalization [65] by plotting $\ln\mathcal{I}_\lambda$. The dashed lines illustrate the second-order case $g_2 = 0$ for two different ω. One sees that the variation of the ground state with λ and therefore the maximal value of $\mathcal{I}_\lambda$ becomes larger for smaller frequencies. The QFI for comparatively large $\omega = 0.1\,\Omega$ shows a broad peak shifted away from the critical point g_s for $\omega = 0$ due to the finite GS extension at finite frequency [19]. The peak becomes sharper at lower frequency and tends to diverge in the limit $\omega \to 0$, as indicated by the dotted red line with $\omega = 0.01\Omega$. At a finite frequency, the QFI does not diverge for

$g_2 = 0$. The situation changes profoundly for non-zero g_2. The GS wave function behaves much more singularly even for $\omega = 0.1 \, \Omega$ (blue solid line), leading to a narrow peak in $\ln \mathcal{I}_\lambda$. Naturally, the maximal QFI is even higher for smaller frequency. By comparing the solid blue and dashed orange lines, we see that the same measurement precision can be obtained if $g_2 \neq 0$ as in the model with $g_2 = 0$, although the mode frequency is an order of magnitude larger. Obviously, the presence of the nonlinear term in H simplifies the requirement to implement the slow-resonator limit.

These features of the QFI can be understood by comparing the behavior of the gap Δ between GS and the first excited state when tuning through the phase transition, shown in Figure 1b. For $g_2 = 0$, the scaled gap Δ/ω goes to zero for $g_1 \gtrsim g_s$. The transition becomes continuous with $\Delta/\omega = 0$ for $g_1 \geq g_s$ in the limit $\omega \to 0$, typical for a second-order transition. Likewise, the GS wave function changes smoothly close to g_s leading to the lower values for the QFI. The closing of the gap means that the dynamical time scale Δ^{-1} diverges in approaching the critical coupling which means that an adiabatic sweep through g_s would be extremely slow for $\omega \approx 0$. This problem will be addressed in the next section.
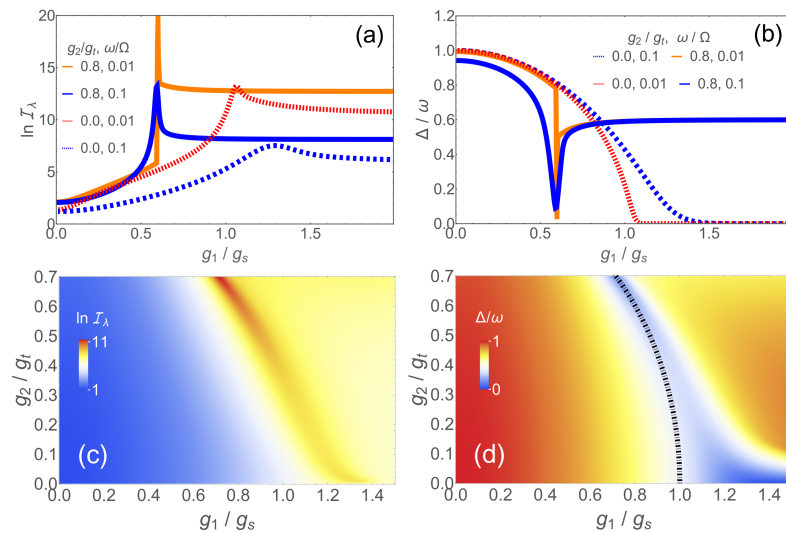

Figure 1. (**a**) $\ln \mathcal{I}_\lambda$ for $\lambda = g_1/\Omega$ and different g_2: $g_2 = 0$ with $\omega/\Omega = 0.01$ (dotted red line) and $\omega/\Omega = 0.01$ (dashed blue line). $g_2/g_t = 0.8$ with $\omega/\Omega = 0.01$ (solid orange line) and $\omega/\Omega = 0.01$ (solid blue line); (**b**) gap Δ/ω for the same parameters as in (**a**); (**c**) $\ln \mathcal{I}_\lambda$ in the g_1/g_2 plane for $\omega/\Omega = 0.1$; and (**d**) gap Δ/ω for the same parameters as in (**c**). The dashed-dotted line represents the phase boundary given in (4).

On the other hand, the gap stays always finite for $g_2 \neq 0$ due to the broken parity symmetry [65], although it changes very fast close to the critical point, even for a large ω, and therefore resembles a first-order transition. This explains the higher QFI in the nonlinear case. The QFI and the gap as a function of g_1 and g_2 are shown in the colorplots of Figure 1c,d for $\omega = 0.1 \, \Omega$. A larger g_2 means a higher maximal QFI, which dramatically increases if g_2 reaches $\sim 0.6 g_s$. In Figure 1c, we only plot up to $g_2 = 0.7 g_t$ as the maximal QFI for a larger $g_2 \approx g_t$ would be out of scale. For these values, the system is close to the point of spectral collapse [59,71–73] where part of the discrete spectrum becomes continuous. Although this regime may not be easily realizable, we see that it has by far the greatest potential with regard to quantum metrology.

4. Preparation Time

The protocol we consider is composed of three steps: first, the system is initialized in its ground state in a region of parameters far from criticality, e.g., $g_1 = 0$, $g_2 < g_t$; then, an adiabatic sweep is performed in order to bring the system in proximity of criticality; finally, a measurement is performed on the system final state. Notice that the ground state is always nondegenerate, even for vanishing values of ω, i.e., the energy gap is always

finite outside the critical region, so the initial and final states are adiabatically connected on any line in the g_1/g_2-plane which does not cross the critical points. To estimate the time needed to perform the adiabatic sweep from $\lambda = 0$ to the intended sensing value λ_s, we may use the condition $d\lambda/dt \ll \Delta(\lambda)$ where $\Delta(\lambda)$ is the energy gap between the ground state and first excited state (see the supplemental material in [15]). This condition gives us an intrinsic lower bound to the time required to adiabatically prepare the system ground state for a given value of λ, even when using an adaptive sweep whose speed of variation is adjusted to the instantaneous value of the energy gap. In this way, we obtain a lower bound for the preparation time

$$T(\lambda_s) \geq \int_0^{\lambda_s} \frac{1}{\Delta(\lambda)} d\lambda. \tag{3}$$

In our present case, we have $\lambda = g_1/\Omega$. In Figure 2, we compare the preparation times for pure linear coupling $g_2 = 0$ (second-order transition) and nonlinear coupling (first-order transition) at the experimentally feasible frequency ratio $\omega/\Omega = 0.1$. While the preparation time seems to diverge at the critical point (which is also the point of maximal QFI) due to critical slowing down in the first case, it stays low in the second. In Figure 2b, we plot the logarithm of $\mathcal{I}_\lambda/(T\Omega)$, a figure of merit to assess the practicability of the sensing protocol. Around the coupling with maximal accuracy, g_m, the system with nonlinear coupling exhibits a precision several orders of magnitude higher than the linear one. In Figure 2c,d, T and $\ln(\mathcal{I}_\lambda/(T\Omega))$ taken at g_m are shown as a function of ω/Ω. The preparation time rises if one approaches the low frequency limit for linear and nonlinear coupling alike because the phase transition features become more pronounced and the gap in the critical region shrinks. Nonetheless, one can see that the preparation time in the presence of nonlinear coupling is much lower than without it. For values above $\omega/\Omega \sim 0.2$, the time does not change much in both cases. Likewise, the "effective accuracy" as measured by $\ln(\mathcal{I}_\lambda/(T\Omega))$ slowly drops for larger values of ω, while the nonlinear system keeps a much higher precision.
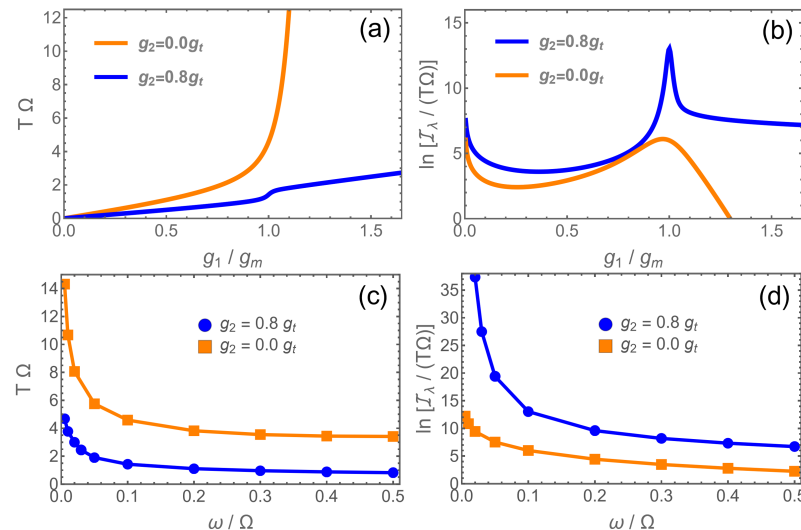

Figure 2. (**a**) Time T needed to prepare the ground state of the system at g_1 for different g_2: $g_2 = 0$ (orange) and $g_2 = 0.8g_t$ (blue), for $\omega = 0.1\,\Omega$. g_m denotes the coupling g_1 with maximal Fisher information $\mathcal{I}_\lambda$. (**b**) $\ln(\mathcal{I}_\lambda/(T\Omega))$ for $g_2 = 0$ (orange) and $g_2 = 0.8g_t$ (blue), for the same parameters as in (**a**). (**c**) Dependence of T at g_m on the mode frequency ω for the two values for g_2 shown in (**a,b**). (**d**) $\ln(\mathcal{I}_\lambda/(T\Omega))$ at g_m as a function of ω for the same parameters as in (**c**).

5. Behavior of the Wave Function

As mentioned above, the high sensitivity of quantum metrology results from the sudden change of the GS wave function $|\psi\rangle$ in the vicinity of the critical point. In Figure 3a,b,

we show the components of $|\psi\rangle = (\psi_+(x), \psi_-(x))^T$ in position space for $g_2 = 0$ and as a function of g_1. The frequency ω is relatively large ($\omega/\Omega = 0.1$) so that the transition is smeared out. Below $g_1 \approx g_s$, both spin components of $|\psi\rangle$ are centered around $x = 0$ which corresponds to unbroken left/right-symmetry. Around g_s, the upper component is displaced to the left and the lower component to the right. This does not mean that the parity symmetry of the model with the Hamiltonian H_0 is broken for $g_1 > g_s$, because the parity operator $e^{i\pi a^\dagger a} \sigma_x$ acts in both spin and position space. Nevertheless, the change in the GS wave function in position space is the analogue of a symmetry breaking quantum phase transition in the QRM. For vanishing nonlinear coupling g_2, the change in both components is smooth, as seen in Figure 3a,b. The situation is quite different if the nonlinear coupling is turned on: for non-zero g_2, which breaks the parity symmetry of H_0, we essentially have the same behavior of $\psi_\pm(x)$ for $g_1 < 0.66g_s$ as in the linear case. However, at $g_1 \approx 0.66g_s$, the wave functions change abruptly: basically, the whole weight is transferred to the right and lower branch $\psi_-(x)$ and the parity symmetry is strongly broken. Of course, this is no symmetry breaking in the usual sense because parity is already broken on the Hamiltonian level. The fast change of $|\psi(x)\rangle$ in tuning through the transition region is responsible for the large QFI, while the gap to the first excited state always remains non-zero.
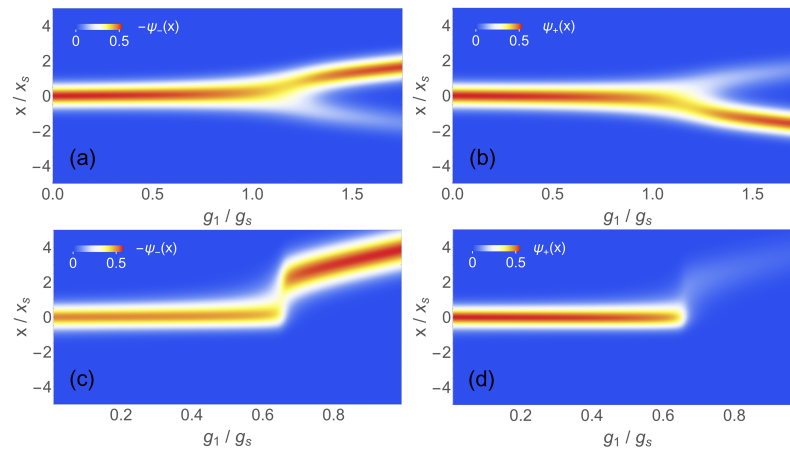

Figure 3. Ground state wave function $\psi_\pm(x)$ for spin component $+$ or $-$ as a function of g_1 at $\omega/\Omega = 0.1$: (**a**) $-\psi_-(x)$ for $g_2 = 0$; (**b**) $\psi_+(x)$ for $g_2 = 0$; (**c**) $\psi_-(x)$ for $g_2 = 0.75g_t$; and (**d**) $\psi_+(x)$ for $g_2 = 0.75g_t$. Here, $x_s = \sqrt{2}g_s/\omega$.

6. Extended Range Quantum Sensing

Up to now, we set the bias ϵ to zero to demonstrate the main differences between the linear and nonlinear models with regard to quantum sensing. From Figure 1c,d, we see that, in varying g_2 between zero and $0.7g_t$, we can drive the critical coupling g_1 which is the quantity to be measured, from g_s to lower values $\sim0.7g_s$, thus extending the range of couplings which can be measured with an accuracy enhanced by criticality. A much larger region of couplings becomes available if the bias ϵ is varied as well which can be easily achieved, e.g., in circuit QED platforms.

In Figure 4a, we show the QFI in the g_1/g_2 plane in the presence of finite bias $\epsilon = 0.1\,\Omega$ at $\omega = 0.1\,\Omega$. The phase transition occurs along the thin red line indicating the sharp maximum of the QFI. The transition line is accurately given by a semi-classical calculation (black dashed line) in closed form as [65]

$$g_{1c}^\epsilon = g_s \left[1 + \frac{g_t \epsilon}{g_2 \Omega}\right]\sqrt{1 - g_2^2/g_t^2}, \tag{4}$$

$$\epsilon_c = \frac{g_2}{g_t}\left[\frac{g_1}{g_s\sqrt{1 - g_2^2/g_t^2}} - 1\right]\Omega. \tag{5}$$

This phase boundary no longer cuts the x axis at a finite value of g_1 as in Figure 1c, but allows for arbitrary large critical values of g_1 for non-zero g_2. The range of accessible couplings is therefore also extended to values above g_s. As such, the whole range $0 < g_1 < \infty$ can be measured with enhanced precision if the couplings g_2 and ϵ are properly tuned.

The QFI has a peak along the phase boundary. This is shown in Figure 4b for various values of g_2. One may notice a shallow maximum of the lines for $g_2/g_t = 0.15$ and 0.25, around $g_1/g_s = 1.2$ before the sharp peak associated with the first order transition. This originates in a second-order transition because the system is located in the vicinity of a tricritical point [65]. However, these maxima only lead to the marginal enhancement of QFI and play no role in the optimal measurement protocol. The contrast between the shallow maximum and the sharp peak for the same g_2 again demonstrates the much higher measurement accuracy made possible by a first-order-like transition compared to a second-order transition.
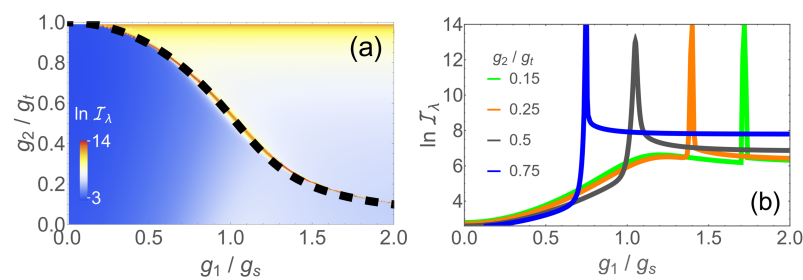

Figure 4. (**a**) $\ln I_\lambda$ in the g_1/g_2 plane at a fixed frequency $\omega/\Omega = 0.1$ and finite bias $\epsilon = 0.1\,\Omega$. The black dashed line denotes the analytic phase boundary where $\mathcal{I}_\lambda$ is maximal; (**b**) $\ln \mathcal{I}_\lambda$ as a function of g_1 for different nonlinear couplings: $g_2/g_t = 0.75$ (blue), 0.5 (dark gray), 0.25 (orange), 0.15 (green).

7. Magnetometry

The general Hamiltonian (1) contains five parameters, all of which can be subjected to quantum metrology. We focused, as an example, to the linear coupling g_1 but other parameters are also interesting from a metrological point of view. The bias ϵ is of particular interest as it can be directly proportional to the intensity of external electric or magnetic fields in atomic and circuit–QED implementations, respectively. Using such a platform, it would be possible to construct a magnetometer analogous to a SQUID with enhanced precision. We computed the QFI for $\lambda = \epsilon/\Omega$ in different parameter regions at finite frequencies. The results are shown in Figure 5b,d as a function of the measured quantity ϵ for non-zero values of g_2 to take advantage of the nonlinear coupling. Qualitatively, we find the same features as for the previous case with $\lambda = g_1/\Omega$. In Figure 5a,c, the phase boundaries are shown in the ϵ/g_1 plane and the ϵ/g_2 plane, respectively. In each case, the whole range for ϵ can be attained by a phase boundary point if g_1 and g_2 are adjusted through a suitable adiabatic preparation process.

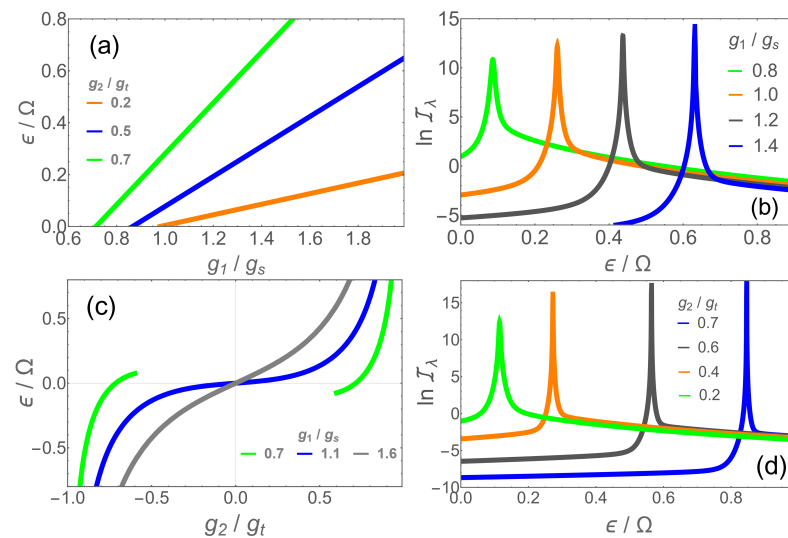**Figure 5.** (**a**) Phase boundaries as a function of g_1 at $g_2/g_t = 0.2$ (orange), 0.5 (blue), 0.7 (green); (**b**) $\ln \mathcal{I}_\lambda$ for $\lambda = \epsilon/\Omega$ as a function of ϵ for $g_2/g_t = 0.7$ and $(g_1/g_s, \omega/\Omega) = (0.8, 0.1)$ (green), $(1.0, 0.2)$ (orange), $(1.2, 0.3)$ (dark gray) and $(1.4, 0.4)$ (blue). (**c**) Phase boundaries as a function of g_2 at $g_1/g_s = 0.7$ (green), 1.1 (blue) and 1.6 (gray). (**d**) $\mathcal{I}_\lambda$ as function of ϵ for $g_1/g_s = 0.7$ at $(g_2/g_t, \omega/\Omega) = (0.2, 0.2)$ (green), $(0.4, 0.2)$ (orange), $(0.6, 0.3)$ (dark gray) and $(0.7, 0.4)$ (blue).

8. Discussion

Via a study of the QFI and the gap of the nonlinear quantum Rabi model with bias, we compared the critical metrology provided by quantum phase transitions of a different order. While the model with only linear coupling shows a transition of second-order type with a closing gap and smooth GS wave function, the transition of the model with additional nonlinear coupling can be classified as first order and featuring a finite gap and a discontinuous change of the GS wave function. The reason for this difference is that the broken parity symmetry of the nonlinear model which manifests itself in the GS wave function only at and above the critical point. In contrast, the linear, parity symmetric model has a GS changing smoothly across the transition. This leads to a dramatic increase in the QFI close to criticality in the nonlinear case. Moreover, the critical slowing down due to the gap closing which extends the preparation time in the linear model is absent for nonlinear coupling. A third advantage of the nonlinear over the linear model is the possibility of avoiding the slow-resonator limit as frequency rations of $\omega/\Omega \sim 0.1$ are sufficient to utilize the critical quantum enhancement of the measurement precision. This condition substantially eases the requirements for an experimental implementation. Finally, adding a standard bias term to the Hamiltonian extends the measurement range for the couplings to all realizable values because the critical point can be shifted by adjusting the bias. On the other hand, one may construct a new type of magnetometer with critically enhanced precision if the bias itself is subjected to the measurement.

Therefore, the extension of the standard quantum Rabi model by including a nonlinear coupling and the bias term may lead to a major improvement of quantum metrology in not just one but several respects.

Author Contributions: Conceptualization, Z.-J.Y., S.F. and D.B.; methodology, Z.-J.Y. and S.F.; formal analysis, Z.-J.Y. and D.B.; software, Z.-J.Y. and G.L.; writing—original draft preparation, Z.-J.Y. and G.L.; writing—review and editing, Z.-J.Y., S.F. and D.B. All authors have read and agreed to the published version of the manuscript.

Institutional Review Board Statement: Not applicable.

Informed Consent Statement: Not applicable.

Data Availability Statement: Not applicable.

Conflicts of Interest: The authors declare no conflict of interest.

References

1. Huang, K. *Statistical Mechanics*; John Wiley & Sons, Inc.: New York, NY, USA, 1987.
2. Täuber, U.C. *Critical Dynamics: A Field Theory Approach to Equilibrium and Non-Equilibrium Scaling Behavior*; Cambridge University Press: Cambridge, UK , 2014. [CrossRef]
3. Pirro, S.; Mauskopf, P. Advances in Bolometer Technology for Fundamental Physics. *Annu. Rev. Nucl. Part. Sci.* **2017**, *67*, 161–181. [CrossRef]
4. Irwin, K.; Hilton, G. Transition-Edge Sensors. In *Cryogenic Particle Detection*; Enss, C., Ed.; Topics in Applied Physics; Springer: Berlin/Heidelberg, Germany, 2005; pp. 63–150. [CrossRef]
5. Degen, C.L.; Reinhard, F.; Cappellaro, P. Quantum sensing. *Rev. Mod. Phys.* **2017**, *89*, 035002. [CrossRef]
6. Sachdev, S. *Quantum Phase Transitions*, 2nd ed.; Cambridge University Press: Cambridge, UK, 2011.
7. Zanardi, P.; Paris, M.G.A.; Campos Venuti, L. Quantum criticality as a resource for quantum estimation. *Phys. Rev. A* **2008**, *78*, 042105. [CrossRef]
8. Invernizzi, C.; Korbman, M.; Campos Venuti, L.; Paris, M.G.A. Optimal quantum estimation in spin systems at criticality. *Phys. Rev. A* **2008**, *78*, 042106. [CrossRef]
9. Ivanov, P.A.; Porras, D. Adiabatic quantum metrology with strongly correlated quantum optical systems. *Phys. Rev. A* **2013**, *88*, 023803. [CrossRef]
10. Bina, M.; Amelio, I.; Paris, M.G.A. Dicke coupling by feasible local measurements at the superradiant quantum phase transition. *Phys. Rev. E* **2016**, *93*, 052118. [CrossRef]
11. Fernández-Lorenzo, S.; Porras, D. Quantum sensing close to a dissipative phase transition: Symmetry breaking and criticality as metrological resources. *Phys. Rev. A* **2017**, *96*, 013817. [CrossRef]
12. Tsang, M. Quantum transition-edge detectors. *Phys. Rev. A* **2013**, *88*, 021801. [CrossRef]
13. Macieszczak, K.; Guţă, M.; Lesanovsky, I.; Garrahan, J.P. Dynamical phase transitions as a resource for quantum enhanced metrology. *Phys. Rev. A* **2016**, *93*, 022103. [CrossRef]
14. Rams, M.M.; Sierant, P.; Dutta, O.; Horodecki, P.; Zakrzewski, J. At the Limits of Criticality-Based Quantum Metrology: Apparent Super-Heisenberg Scaling Revisited. *Phys. Rev. X* **2018**, *8*, 021022. [CrossRef]
15. Garbe, L.; Bina, M.; Keller, A.; Paris, M.G.A.; Felicetti, S. Critical Quantum Metrology with a Finite-Component Quantum Phase Transition. *Phys. Rev. Lett.* **2020**, *124*, 120504. [CrossRef]
16. Bakemeier, L.; Alvermann, A.; Fehske, H. Quantum phase transition in the Dicke model with critical and noncritical entanglement. *Phys. Rev. A* **2012**, *85*, 043821. [CrossRef]
17. Ashhab, S. Superradiance transition in a system with a single qubit and a single oscillator. *Phys. Rev. A* **2013**, *87*, 013826. [CrossRef]
18. Hwang, M.J.; Puebla, R.; Plenio, M.B. Quantum Phase Transition and Universal Dynamics in the Rabi Model. *Phys. Rev. Lett.* **2015**, *115*, 180404. [CrossRef] [PubMed]
19. Ying, Z.J.; Liu, M.; Luo, H.G.; Lin, H.Q.; You, J.Q. Ground-state phase diagram of the quantum Rabi model. *Phys. Rev. A* **2015**, *92*, 053823. [CrossRef]
20. Liu, M.; Chesi, S.; Ying, Z.J.; Chen, X.; Luo, H.G.; Lin, H.Q. Universal Scaling and Critical Exponents of the Anisotropic Quantum Rabi Model. *Phys. Rev. Lett.* **2017**, *119*, 220601. [CrossRef]
21. Puebla, R.; Hwang, M.J.; Plenio, M.B. Excited-state quantum phase transition in the Rabi model. *Phys. Rev. A* **2016**, *94*, 023835. [CrossRef]
22. Puebla, R.; Hwang, M.J.; Casanova, J.; Plenio, M.B. Probing the dynamics of a superradiant quantum phase transition with a single trapped ion. *Phys. Rev. Lett.* **2017**, *118*, 073001. [CrossRef]
23. Hwang, M.J.; Rabl, P.; Plenio, M.B. Dissipative phase transition in the open quantum Rabi model. *Phys. Rev. A* **2018**, *97*, 013825. [CrossRef]
24. Zhu, H.J.; Xu, K.; Zhang, G.F.; Liu, W.M. Finite-Component Multicriticality at the Superradiant Quantum Phase Transition. *Phys. Rev. Lett.* **2020**, *125*, 050402. [CrossRef]
25. Puebla, R. Finite-component dynamical quantum phase transitions. *Phys. Rev. B* **2020**, *102*, 220302(R). [CrossRef]
26. Ying, Z.J. From Quantum Rabi Model To Jaynes-Cummings Model: Symmetry-Breaking Quantum Phase Transitions, Symmetry-Protected Topological Transitions and Multicriticality. *Adv. Quantum Technol.* **2022**, *5*, 2100088. [CrossRef]
27. Ying, Z.J. Hidden Single-Qubit Topological Phase Transition without Gap Closing in Anisotropic Light-Matter Interactions. *Adv. Quantum Technol.* **2022**, *5*, 2100165. [CrossRef]
28. Liu, J.; Liu, M.; Ying, Z.J.; Luo, H.G. Fundamental Models in the Light-Matter Interaction: Quantum Phase Transitions and the Polaron Picture. *Adv. Quantum Technol.* **2021**, *4*, 2000139. [CrossRef]
29. Casteels, W.; Fazio, R.; Ciuti, C. Critical dynamical properties of a first-order dissipative phase transition. *Phys. Rev. A* **2017**, *95*, 012128. [CrossRef]

30. Bartolo, N.; Minganti, F.; Casteels, W.; Ciuti, C. Exact steady state of a Kerr resonator with one- and two-photon driving and dissipation: Controllable Wigner-function multimodality and dissipative phase transitions. *Phys. Rev. A* **2016**, *94*, 033841. [CrossRef]

31. Minganti, F.; Biella, A.; Bartolo, N.; Ciuti, C. Spectral theory of Liouvillians for dissipative phase transitions. *Phys. Rev. A* **2018**, *98*, 042118. [CrossRef]

32. Peng, J.; Rico, E.; Zhong, J.; Solano, E.; Egusquiza, I.L. Unified superradiant phase transitions. *Phys. Rev. A* **2019**, *100*, 063820. [CrossRef]

33. Felicetti, S.; Le Boité, A. Universal Spectral Features of Ultrastrongly Coupled Systems. *Phys. Rev. Lett.* **2020**, *124*, 040404. [CrossRef]

34. Kewming, M.J.; Mitchison, M.T.; Landi, G.T. Diverging current fluctuations in critical Kerr resonators. *arXiv* **2022**, arXiv:2205.02622.

35. Ivanov, P.A. Enhanced two-parameter phase-space-displacement estimation close to a dissipative phase transition. *Phys. Rev. A* **2020**, *102*, 052611. [CrossRef]

36. Chu, Y.; Zhang, S.; Yu, B.; Cai, J. Dynamic Framework for Criticality-Enhanced Quantum Sensing. *Phys. Rev. Lett.* **2021**, *126*, 010502. [CrossRef] [PubMed]

37. Gietka, K.; Metz, F.; Keller, T.; Li, J. Adiabatic critical quantum metrology cannot reach the Heisenberg limit even when shortcuts to adiabaticity are applied. *Quantum* **2021**, *5*, 489. [CrossRef]

38. Hu, Y.; Huang, J.; Huang, J.F.; Xie, Q.T.; Liao, J.Q. Dynamic sensitivity of quantum Rabi model with quantum criticality. *arXiv* **2021**, arXiv:2101.01504.

39. Liu, R.; Chen, Y.; Jiang, M.; Yang, X.; Wu, Z.; Li, Y.; Yuan, H.; Peng, X.; Du, J. Experimental Adiabatic Quantum Metrology with the Heisenberg scaling. *arXiv* **2021**, arXiv:2102.07056.

40. Ilias, T.; Yang, D.; Huelga, S.F.; Plenio, M.B. Criticality-Enhanced Quantum Sensing via Continuous Measurement. *PRX Quantum* **2022**, *3*, 010354. [CrossRef]

41. Frérot, I.; Roscilde, T. Quantum Critical Metrology. *Phys. Rev. Lett.* **2018**, *121*, 020402. [CrossRef]

42. Heugel, T.L.; Biondi, M.; Zilberberg, O.; Chitra, R. Quantum Transducer Using a Parametric Driven-Dissipative Phase Transition. *Phys. Rev. Lett.* **2019**, *123*, 173601. [CrossRef]

43. Mirkhalaf, S.S.; Witkowska, E.; Lepori, L. Supersensitive quantum sensor based on criticality in an antiferromagnetic spinor condensate. *Phys. Rev. A* **2020**, *101*, 043609. [CrossRef]

44. Wald, S.; Moreira, S.V.; Semião, F.L. In- and out-of-equilibrium quantum metrology with mean-field quantum criticality. *Phys. Rev. E* **2020**, *101*, 052107. [CrossRef]

45. Ivanov, P.A. Steady-state force sensing with single trapped ion. *Phys. Scr.* **2020**, *95*, 025103. [CrossRef]

46. Salado-Mejía, M.; Román-Ancheyta, R.; Soto-Eguibar, F.; Moya-Cessa, H.M. Spectroscopy and critical quantum thermometry in the ultrastrong coupling regime. *Quantum Sci. Technol.* **2021**, *6*, 025010. [CrossRef]

47. Niezgoda, A.; Chwedeńczuk, J. Many-Body Nonlocality as a Resource for Quantum-Enhanced Metrology. *Phys. Rev. Lett.* **2021**, *126*, 210506. [CrossRef] [PubMed]

48. Mishra, U.; Bayat, A. Integrable quantum many-body sensors for AC field sensing. *arXiv* **2021**, arXiv:2105.13507.

49. Garbe, L.; Abah, O.; Felicetti, S.; Puebla, R. Exponential precision by reaching a quantum critical point. *arXiv* **2021**, arXiv:2112.11264.

50. Gietka, K. Squeezing by critical speeding up: Applications in quantum metrology. *Phys. Rev. A* **2022**, *105*, 042620. [CrossRef]

51. Gietka, K.; Ruks, L.; Busch, T. Understanding and Improving Critical Metrology. Quenching Superradiant Light-Matter Systems Beyond the Critical Point. *Quantum* **2022**, *6*, 700. [CrossRef]

52. Di Candia, R.; Minganti, F.; Petrovnin, K.V.; Paraoanu, G.S.; Felicetti, S. Critical parametric quantum sensing. *arXiv* **2021**, arXiv:2107.04503.

53. Montenegro, V.; Mishra, U.; Bayat, A. Global Sensing and Its Impact for Quantum Many-Body Probes with Criticality. *Phys. Rev. Lett.* **2021**, *126*, 200501. [CrossRef]

54. Garbe, L.; Abah, O.; Felicetti, S.; Puebla, R. Critical quantum metrology with fully-connected models: From Heisenberg to Kibble–Zurek scaling. *Quantum Sci. Technol.* **2022**, *7*, 035010. [CrossRef]

55. Rabi, I.I. Space quantization in a gyrating magnetic field. *Phys. Rev.* **1937**, *51*, 652–654. [CrossRef]

56. Jaynes, E.T.; Cummings, F.W. Comparison of quantum and semiclassical radiation theories with application to the beam maser. *Proc. IEEE* **1963**, *51*, 89–109. [CrossRef]

57. Braak, D.; Chen, Q.H.; Batchelor, M.T.; Solano, E. Semi-classical and quantum Rabi models: In celebration of 80 years. *J. Phys. A Math. Theor.* **2016**, *49*, 300301. [CrossRef]

58. Bertet, P.; Chiorescu, I.; Harmans, C.J.P.M.; Mooij, J.E. Dephasing of a flux-qubit coupled to a harmonic oscillator. *arXiv* **2005**, arXiv:cond-mat/0507290.

59. Felicetti, S.; Pedernales, J.S.; Egusquiza, I.L.; Romero, G.; Lamata, L.; Braak, D.; Solano, E. Spectral collapse via two-phonon interactions in trapped ions. *Phys. Rev. A* **2015**, *92*, 033817. [CrossRef]

60. Puebla, R.; Hwang, M.J.; Casanova, J.; Plenio, M.B. Protected ultrastrong coupling regime of the two-photon quantum Rabi model with trapped ions. *Phys. Rev. A* **2017**, *95*, 063844. [CrossRef]

61. Cong, L.; Felicetti, S.; Casanova, J.; Lamata, L.; Solano, E.; Arrazola, I. Selective interactions in the quantum Rabi model. *Phys. Rev. A* **2020**, *101*, 032350. [CrossRef]

62. Felicetti, S.; Rossatto, D.Z.; Rico, E.; Solano, E.; Forn-Díaz, P. Two-photon quantum Rabi model with superconducting circuits. *Phys. Rev. A* **2018**, *97*, 013851. [CrossRef]

63. Felicetti, S.; Hwang, M.J.; Le Boité, A. Ultrastrong-coupling regime of nondipolar light-matter interactions. *Phys. Rev. A* **2018**, *98*, 053859. [CrossRef]

64. Sánchez Muñoz, C.; Frisk Kockum, A.; Miranowicz, A.; Nori, F. Simulating ultrastrong-coupling processes breaking parity conservation in Jaynes-Cummings systems. *Phys. Rev. A* **2020**, *102*, 033716. [CrossRef]

65. Ying, Z.J. Symmetry-breaking patterns, tricriticalities, and quadruple points in the quantum Rabi model with bias and nonlinear interaction. *Phys. Rev. A* **2021**, *103*, 063701. [CrossRef]

66. Mooij, J.E.; Orlando, T.P.; Levitov, L.; Tian, L.; van der Wal, C.H.; Lloyd, S. Josephson Persistent-Current Qubit. *Science* **1999**, *285*, 1036. [CrossRef] [PubMed]

67. Zheng, R.H.; Ning, W.; Chen, Y.H.; Lu, J.H.; Shen, L.T.; Xu, K.; Zhang, Y.R.; Xu, D.; Li, H.; Xia, Y.; et al. Emergent Schrodinger cat states during superradiant phase transitions. *arXiv* **2022**, arXiv:2207.05512.

68. Ying, Z.J.; Cong, L.; Sun, X.M. Quantum phase transition and spontaneous symmetry breaking in a nonlinear quantum Rabi model. *J. Phys. A Math. Theor.* **2020**, *53*, 345301. [CrossRef]

69. Lo, C.F.; Liu, K.L.; Ng, K.M. The multiquantum Jaynes-Cummings model with the counter-rotating terms. *Europhys. Lett.* **1998**, *42*, 1. [CrossRef]

70. Duan, L.; Xie, Y.F.; Braak, D.; Chen, Q.H. Two-photon Rabi model: Analytic solutions and spectral collapse. *J. Phys. A Math. Theor.* **2016**, *49*, 464002. [CrossRef]

71. Garbe, L.; Egusquiza, I.L.; Solano, E.; Ciuti, C.; Coudreau, T.; Milman, P.; Felicetti, S. Superradiant phase transition in the ultrastrong-coupling regime of the two-photon Dicke model. *Phys. Rev. A* **2017**, *95*, 053854. [CrossRef]

72. Cong, L.; Sun, X.M.; Liu, M.; Ying, Z.J.; Luo, H.G. Polaron picture of the two-photon quantum Rabi model. *Phys. Rev. A* **2019**, *99*, 013815. [CrossRef]

73. Braak, D. Spectral determinant of the two-photon quantum Rabi model. *arXiv* **2022**, arXiv:2206.02509.

74. Braunstein, S.L.; Caves, C.M. Statistical distance and the geometry of quantum states. *Phys. Rev. Lett.* **1994**, *72*, 3439–3443. [CrossRef]

75. Taddei, M.M.; Escher, B.M.; Davidovich, L.; de Matos Filho, R.L. Quantum Speed Limit for Physical Processes. *Phys. Rev. Lett.* **2013**, *110*, 050402. [CrossRef] [PubMed]